INTERNATIONAL JOURNAL FOR NUMERICAL METHODS IN FLUIDS, VOL. 16, 1007–1025 (1993)

TURBULENT FREE SURFACE FLOW SIMULATION USING A MULTILAYER MODEL

C. J. LAI AND C. W. YEN

Department of Hydraulic and Ocean Engineering, Cheng-Kung University, Tainan, Taiwan, ROC.

SUMMARY

Based on the steady hydrodynamic equations, a multilayer (ML) model has been formulated for simulating turbulent flow in open channels. The model is imposed on a general curvilinear co-ordinate system with non-staggered finite volume discretization. The turbulent quantities in the model are described by the layer-averaged k–ε turbulence model with standard coefficients. Assuming a vertical hydrostatic pressure distribution, a depth correction scheme, originating in the Rhie and Chow approach for confined flows, is incorporated into the SIMPLE procedure to compute the water surface.

Using the multilayer model, flows in a 180° channel bend, near a groin, and in straight open channels are computed. The results are compared with experimental data and with calculations of a depth-averaged model (DAV) having three-dimensional effect corrections. The comparisons show that the predictions of the ML model on mean flow values are in good agreement with the available data and are better than those of the DAV model. The vertical distribution of the turbulent energy dissipation rate is also shown to agree well with the open-channel measurements.

KEY WORDS Multilayer model k–ε model of turbulence Free surface Recirculating flow Curvilinear co-ordinates Non-staggered grid Depth correction scheme

1. INTRODUCTION

Turbulent flows in hydraulic engineering applications of various length scales have many forms. Several numerical models using rectangular or curvilinear grids have been developed[1–4] to simulate these flows. The depth-averaged k–ε turbulence model is the most widely used model in describing the turbulent properties of the flows. For small or laboratory-scale channels, the depth-averaged k–ε turbulence model proposed by Rastogi and Rodi[5] had been used by Keller and Rodi,[6] McGuirk and Rodi,[7] Lai *et al.*[8] and Tingsanchali and Maheswaran[9] to compute flow in compound channel, channel flow with a side discharge and channel flow near a groin. For flow in large or practical scales, Raithby *et al.*[10] used orthogonal curvilinear co-ordinates in the horizontal direction, and σ-co-ordinates in the vertical direction, to predict thermal discharge in a coastal region. The flows predicted in these studies are generally good, except when recirculating patterns exist. An ASCE review committee[2] recognized that the recirculating zone can be underestimated due to the insufficient capability of the standard k–ε turbulence model.

To improve the accuracy of the two-dimensional (2D) models in predicting recirculating flows, several correction procedures have been used—the correction for the streamline curvature,[11,12] the correction for the friction coefficient of the three-dimensional (3D) effect,[13] and the modification of the eddying term in the energy dissipation equation,[8] etc. Unfortunately, these modifications require several empirical constants, which depend on flow types and must be determined by experimenting or calibrating.

0271–2091/93/111007–19$14.50

Received February 1992
Revised January 1993

Since recirculating flow is three-dimensional in nature, intuitively one would think that a full 3D model can give the best prediction. However, a full 3D model requires the determination of the free surface from kinematic and dynamic boundary conditions and requires more sophisticated computation. To reduce this computational difficulty, some investigators[14–16] used the 'rigid-lid' assumption on the free surface, but others, such as Lardier and Cekirge,[17] and Shimizu *et al.*,[18] coupled the shallow-water and full 3D models to obtain the free-surface elevation and the 3D flow field. In these 3D hydrodynamic model, the eddy viscosity within the governing equations was estimated with empirical profiles.[19,20] Since these profiles were not universal, different empirical vertical eddy viscosity profiles produce different numerical results.

Attempting to improve the prediction of flows, we have developed a hydrodynamic multilayered turbulent flow (ML) model. This model uses the SIMPLE algorithm,[21] incorporates the k–ε turbulence model, specifies the bed and wall shear stresses with wall function and relieves the 'rigid-lid' assumption on the free surface. For versatile applications, the model has used the boundary-fitted co-ordinate system with a non-staggered grid arrangement. The use of the turbulence model in multilayer form and the modification of the pressure correction procedure of Rhie and Chow[22] for the water surface correction are the contributions of the present paper. The formulation and solution algorithm are discussed in the next two sections. The model is validated by comparing the computed mean flow and turbulent quantities with those obtained from the laboratory experiments.

2. GOVERNING EQUATIONS

Multilayer mean flow equations

The following assumptions are made in the present model:

(1) The mean flow field is in steady state.
(2) The vertical pressure distribution is hydrostatic.
(3) The turbulent Reynolds stresses can be approximated by the Boussinesq eddy-viscosity concept.
(4) The vertical distribution of the flow quantities within a layer is nearly uniform.
(5) Layer interfaces, except the free surface, are parallel to the mean water level.

By integrating the 3D continuity and the Reynolds equations over the thickness of each layer shown in Figure 1, the layer-averaged mean flow equations for steady-state incompressible flow are derived as

$$\sum_{l=1}^{l_{max}} \left[\frac{\partial}{\partial x}(\rho h\bar{u})_l + \frac{\partial}{\partial y}(\rho h\bar{v})_l \right] = 0, \tag{1}$$

$$\frac{\partial}{\partial x}(\rho h\bar{u})_l + \frac{\partial}{\partial y}(\rho h\bar{v})_l + (\rho w)_l - (\rho w)_b = 0, \tag{2}$$

$$\frac{\partial}{\partial x}(\rho h\bar{u}\bar{u})_l + \frac{\partial}{\partial y}(\rho h\bar{u}\bar{v})_l = \frac{\partial}{\partial x}(h\bar{\tau}_{xx})_l + \frac{\partial}{\partial y}(h\bar{\tau}_{xy})_l - \rho_l g h_l \frac{\partial}{\partial x} H + S_u, \tag{3}$$

$$\frac{\partial}{\partial x}(\rho h\bar{u}\bar{v})_l + \frac{\partial}{\partial y}(\rho h\bar{v}\bar{v})_l = \frac{\partial}{\partial x}(h\bar{\tau}_{xy})_l + \frac{\partial}{\partial y}(h\bar{\tau}_{yy})_l - \rho_l g h_l \frac{\partial}{\partial y} H + S_v. \tag{4}$$

Equations (1) and (2) are the continuity equations for the entire channel and each layer. Equations (3) and (4) are the x (longitudinal) and y (transverse) momentum equations for each

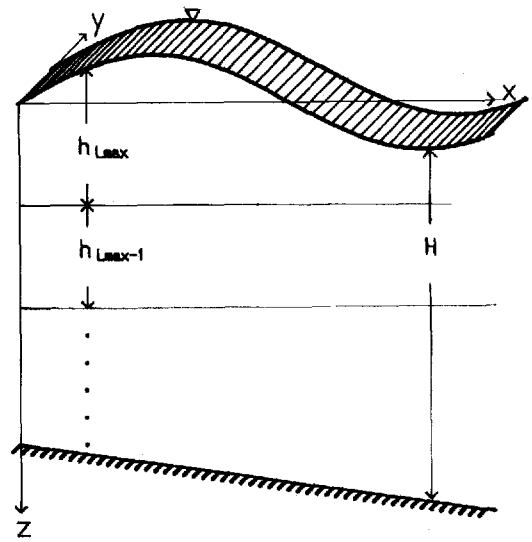

Figure 1. Multilayer open-channel flow system

layer, in which u and v are the horizontal layer-averaged mean velocities and w is the vertical velocity specified at the interface of each layer. The subscripts l, t, b, denote the index of a layer, the top and the bottom surfaces of the layer, respectively. Using these notations, a depth-averaged model is a single-layer model, and the layer surface velocities at t and b are zero.

The eddy viscosity μ_t and the turbulent stress τ_{xx}, τ_{xy} at each layer are determined from the k–ε turbulence model. The present layer-averaged k–ε turbulence model is based on the depth-averaged form of Rostogi and Rodi,[5] with one extra source term added to consider the convective and diffusive effects tht exist between the layers. According to the Boussinesq's concept, the turbulent shear stress can be expressed in Cartesian tensor notation as

$$\bar{\tau}_{ij}=\bar{\mu}_t\left(\frac{\partial \bar{u}_i}{\partial x_j}+\frac{\partial \bar{u}_j}{\partial x_i}\right)-\frac{2}{3}\rho\bar{k}\delta_{ij}. \tag{5}$$

The turbulent viscosity μ_t is expressed in terms of the layer-averaged turbulent kinetic energy k and dissipation rate ε as

$$\bar{\mu}_t=\frac{C_\mu \rho \bar{k}^2}{\bar{\varepsilon}}. \tag{6}$$

So the source terms in equations (4) and (5) are written as

$$S_u=\mu_t\left(\frac{\partial u}{\partial z}+\frac{\partial w}{\partial x}\right)_t-\mu_t\left(\frac{\partial u}{\partial z}+\frac{\partial w}{\partial x}\right)_b-(\rho wu)_t+(\rho wu)_b \tag{7}$$

and

$$S_v=\mu_t\left(\frac{\partial v}{\partial z}+\frac{\partial w}{\partial y}\right)_t-\mu_t\left(\frac{\partial v}{\partial z}+\frac{\partial w}{\partial y}\right)_b-(\rho wv)_t+(\rho wv)_b \tag{8}$$

The turbulence quantities k and ε for each layer are determined from the solution of the following

transport equations:

$$\frac{\partial}{\partial x}(\rho h\bar{u}\bar{k})+\frac{\partial}{\partial y}(\rho h\bar{v}\bar{k})=\frac{\partial}{\partial x}\left(h\frac{\bar{\mu}_t}{\sigma_k}\frac{\partial\bar{k}}{\partial x}\right)+\frac{\partial}{\partial y}\left(h\frac{\bar{\mu}_t}{\sigma_k}\frac{\partial\bar{k}}{\partial y}\right)+hG-h\bar{\varepsilon}+hP_{kv}+S_k \tag{9}$$

and

$$\frac{\partial}{\partial x}(\rho h\bar{u}\bar{\varepsilon})+\frac{\partial}{\partial y}(\rho h\bar{v}\bar{\varepsilon})=\frac{\partial}{\partial x}\left(h\frac{\bar{\mu}_t}{\sigma_\varepsilon}\frac{\partial\bar{\varepsilon}}{\partial x}\right)+\frac{\partial}{\partial y}\left(h\frac{\bar{\mu}_t}{\sigma_\varepsilon}\frac{\partial\bar{\varepsilon}}{\partial y}\right)+C_1\frac{\bar{\varepsilon}}{\bar{k}}hG-\rho C_2 h\frac{\bar{\varepsilon}^2}{\bar{k}}+hP_{k\varepsilon}+S_\varepsilon, \tag{10}$$

where

$$S_k=\left(\frac{\mu_t}{\sigma_k}\frac{\partial\bar{k}}{\partial z}\right)_t-\left(\frac{\mu_t}{\sigma_k}\frac{\partial\bar{k}}{\partial z}\right)_b-(\rho wk)_t+(\rho wk)_b \tag{11}$$

and

$$S_\varepsilon=\left(\frac{\mu_t}{\sigma_\varepsilon}\frac{\partial\bar{\varepsilon}}{\partial z}\right)_t-\left(\frac{\mu_t}{\sigma_\varepsilon}\frac{\partial\bar{\varepsilon}}{\partial z}\right)_b-(\rho w\varepsilon)_t+(\rho w\varepsilon)_b \tag{12}$$

In equations (9) and (10), G is the production term for turbulent kinetic energy of each layer and can be expressed as

$$G=\mu_t\left[2\left(\frac{\partial\bar{u}}{\partial x}\right)^2+2\left(\frac{\partial\bar{v}}{\partial y}\right)^2+2\left(\frac{\partial w}{\partial z}\right)^2+\left(\frac{\partial\bar{u}}{\partial y}+\frac{\partial\bar{v}}{\partial x}\right)^2+\left(\frac{\partial\bar{u}}{\partial z}+\frac{\partial w}{\partial x}\right)^2+\left(\frac{\partial\bar{v}}{\partial z}+\frac{\partial w}{\partial y}\right)^2\right]. \tag{13}$$

In equation (10), P_{kv} and $P_{k\varepsilon}$ are source terms which absorb the effects of the non-uniform vertical distributions of k and ε. At the bottom layer ($l=1$) or for the depth-averaged model ($l_{max}=1$), these two terms can be expressed as:[6]

$$P_{kv}=\frac{\rho}{\sqrt{C_f}}\frac{U_{b*}^3}{h}, \qquad l=1 \tag{14}$$

and

$$P_{k\varepsilon}=3{\cdot}6\rho\frac{C_2}{C_f^{3/4}}\sqrt{C_\mu}\frac{U_{b*}^4}{h^2}, \tag{15}$$

where C_f and U_{b*} are the friction coefficient and friction velocity at channel bed, respectively. In the present multilayer model the values of P_{kv} and $P_{k\varepsilon}$ at each layer are set to zero, and the wall function expression is used at the lowest layer. The values of the empirical constants are: $C_\mu=0{\cdot}09$, $C_1=1{\cdot}43$, $C_2=1{\cdot}92$, $\sigma_k=1{\cdot}0$ and $\sigma_\varepsilon=1{\cdot}3$. All the quantities are specified at the middle depth of the layer. The quantity at interface is linearly interpolated from those at adjoining upper and lower layers.

Boundary conditions

The boundary conditions are required at upstream and downstream locations, at the bottom and at the free surface. At the upstream location the fully developed values for the velocities, k and ε are specified. At the downstream location a fully developed zero-gradient condition is used.

At the side walls and channel bed, non-penetrating conditions are applied. Also, the wall function of Launder and Spalding[23] is employed to link the velocities at the first grid point or at the bottom layer to the boundary shear stresses. The values of $\bar{k}$ and $\bar{\varepsilon}$ near the boundaries are

also calculated by applying the empirical formulas proposed by Rastogi and Rodi. For example, the values of $\bar{k}$ and $\bar{\varepsilon}$ at the centre of the first grid can be calculated from

$$\bar{k}=\frac{U_{w*}^2}{\sqrt{C_\mu}}, \qquad \bar{\varepsilon}=\frac{U_{w*}^3}{\kappa y_w}, \qquad y_w^+=\frac{U_w y_w}{v}\geq 11{\cdot}0, \tag{16}$$

$$\tau_w=\rho\kappa C_\mu^{1/4}k^{1/2}\frac{U_p}{\ln(Ey_w^+)},$$

where y_w is the distance from the wall, κ is the von Karman constant and U_p is the estimated velocity parallel to the wall. E is related to the boundary roughness and is equal to 9·0 for the smooth wall.

At the free surface (the upper face of the top layer), mean velocities u, v and turbulent kinetic energy k are extrapolated from the layers near the surface. Velocity normal to the free surface is set to zero and ε is obtained from the expression given by Noat and Rodi[15] as

$$\varepsilon_s=\frac{C_\mu^{1/4}}{\kappa}k_s^{3/2}\left(\frac{1}{y_o}+\frac{1}{y_w}\right), \tag{17}$$

where y_o is called the 'virtual origin' and s represents the value at the free surface. Based on the evaluation of Noat and Rodi, a value of 0·07 times the local depth H can be used to represent y_o. The water depth near the solid wall is extrapolated from the depth at the nearby grid points.

3. SOLUTION ALGORITHM

Transformation of governing equations

Omitting the subscript l denoting the layer number and the overbar, denoting the layer-averaged values, the transport equations of the variables for each layer given in the last section can be rewritten in a general form as

$$\frac{\partial}{\partial x}(\rho hu\phi)+\frac{\partial}{\partial y}(\rho hv\phi)=\frac{\partial}{\partial x}\left(h\Gamma_\phi\frac{\partial\phi}{\partial x}\right)+\frac{\partial}{\partial y}\left(h\Gamma_\phi\frac{\partial\phi}{\partial y}\right)+R_\phi, \tag{18}$$

where $\phi=1, u, v, k$ or ε and Γ_ϕ is the effective diffusion coefficient. R_ϕ is the source term in equations (3), (4), (9) and (10).

By introducing a curvilinear co-ordinate system (ξ, η) and the relationship between the physical and the transformed planes shown in Figure 2, equation (18) is transformed into (ξ, η) co-ordinates and written as

$$\frac{1}{J}\frac{\partial}{\partial\xi}(J\rho hU\phi)+\frac{1}{J}\frac{\partial}{\partial\eta}(J\rho hV\phi)=\frac{1}{J}\frac{\partial}{\partial\xi}\left(Jg^{11}h\Gamma_\phi\frac{\partial\phi}{\partial\xi}\right)+\frac{1}{J}\frac{\partial}{\partial\eta}\left(Jg^{22}\Gamma_\phi\frac{\partial\phi}{\partial\eta}\right)+S_\phi, \tag{19}$$

where the source term S_ϕ is defined as

$$S_\phi=R_\phi+\frac{1}{J}\frac{\partial}{\partial\xi}\left(Jg^{12}h\Gamma_\phi\frac{\partial\phi}{\partial\eta}\right)+\frac{1}{J}\frac{\partial}{\partial\eta}\left(Jg^{21}\Gamma_\phi\frac{\partial\phi}{\partial\xi}\right) \tag{20}$$

The contravariant velocity components U and V are related to the Cartesian velocity components u and v by the Jacobian J by

$$U=\frac{1}{J}(uy_\eta-vx_\eta) \tag{21}$$

and

$$V=\frac{1}{J}(-uy_\xi+vx_\xi). \tag{22}$$

Jacobian J and the metric tensor components g^{11}, g^{12}, g^{21} and g^{22} are defined as

$$J=x_\xi y_\eta-x_\eta y_\xi, \tag{23}$$

$$g^{11}=\frac{1}{J^2}(x_\eta^2+y_\eta^2), \qquad g^{22}=\frac{1}{J^2}(x_\xi^2+y_\xi^2) \tag{24}$$

and

$$g^{12}=g^{21}=-\frac{1}{J^2}(x_\xi x_\eta+y_\xi y_\eta) \tag{25}$$

Numerical discretization

The discretized form of the governing equations for each layer is obtained by integrating ϕ over a control volume of a typical grid point P (see Figure 2), using the adjacent grid points to the north(N), south(S), east(E) and west(W) and assuming a stepwise variation for variable ϕ between point P and the adjacent grid points. To find the flux at the faces of control volume, the power-law scheme[21] is adopted. The discretized equations are arranged as follows:

Equation of continuity (for each layer):

$$(J\rho hU\Delta\eta)_e-(J\rho hU\Delta\eta)_w+(J\rho hV\Delta\xi)_n-(J\rho hV\Delta\xi)_s+(J\rho w\Delta\xi\Delta\eta)_t-(J\rho w\Delta\xi\Delta\eta)_b=0 \tag{26}$$

Equation for the overall depth:

$$\sum_{l=1}^{l_{max}}[(J\rho hU\Delta\eta)_e-(J\rho hU\Delta\eta)_w+(J\rho hV\Delta\xi)_n-(J\rho hV\Delta\xi)_s]=0. \tag{27}$$

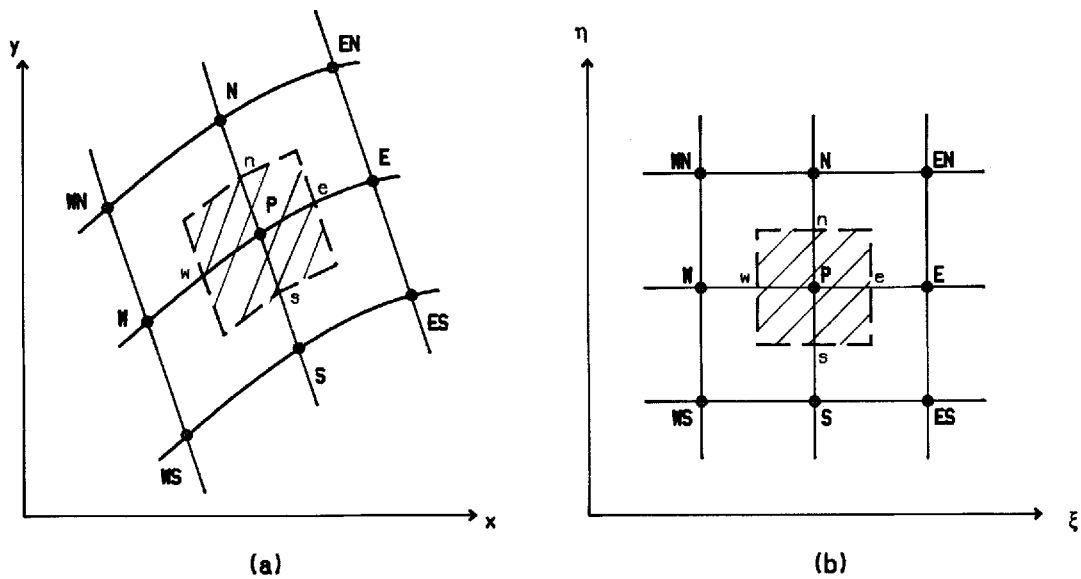

Figure 2. Non-staggered control volume: (a) physical and (b) computational domains

The equations of motion in the x and y directions for each layer are written as

$$u_p=\frac{1}{A_p^u}\left[\sum_{n=E,W,N,S} A_n^u u_n+S^u\right]+h(B^u H_\xi+C^u H_\eta) \tag{28}$$

and

$$v_p=\frac{1}{A_p^v}\left[\sum_{n=E,W,N,S} A_n^v v_n+S^v\right]+h(B^v H_\xi+C^v H_\eta), \tag{29}$$

respectively, where

$$B^u=-\rho g\frac{y_\eta}{A_p^u}\Delta\xi\,\Delta\eta, \qquad C^u=\rho g\frac{y_\xi}{A_p^u}\Delta\xi\,\Delta\eta \tag{30}$$

and

$$B^v=\rho g\frac{x_\eta}{A_p^v}\Delta\xi\,\Delta\eta, \qquad C^v=-\rho g\frac{x_\xi}{A_p^v}\Delta\xi\,\Delta\eta. \tag{31}$$

In equations (28) and (29) u_p and v_p are the layer-averaged velocities and S^u and S^v are the source terms, which exclude the pressure gradients, at point P in the x and y directions, respectively. The 'n' summations are taken over the adjacent grid points (E, W, N and S).

Water depth correction equation

The velocity components u and v can be solved from the momentum equations for each layer. In general, u and v are the estimated values and do not satisfy mass conservation unless both the local water depth and the thickness of each layer are correct in the physical domain. The local water depth correction H' and the layer thickness correction h' are introduced to satisfy both the momentum and the continuity equations. The correct flow field (u, v, h, H) for each layer are obtained from the current estimates of u^*, v^*, h^* and H^* by the addition of the correction values (u', v', h', H') as

$$\begin{aligned} u&=u^*+u', \qquad v=v^*+v',\\ h&=h^*+h', \qquad H=H^*+H'. \end{aligned} \tag{32}$$

If u^* is the layer-averaged velocity based on H^* and h^*, then it is written as

$$u_p^*=\frac{1}{A_p^u}\left[\sum_{n=E,W,N,S} A_n^u u_n^*+S^u\right]+h^*(B^u H_\xi^*+C^u H_\eta^*). \tag{33}$$

Substituting equation (33) into equation (28), the velocity correction u_p' is obtained as

$$u_p'=\frac{1}{A_p^u}\left[\sum_{n=E,W,N,S} A_n^u u_n'\right]+h^*(B^u H_\xi'+C^u H_\eta')+h'(B^u H_\xi^*+C^u H_\eta^*)+h'(B^u H_\xi'+C^u H_\eta'). \tag{34}$$

The first term on the right-hand side of this equation may be dropped without affecting the converged solution.[21] h' is set to zero for each layer except the top layer l_{max} which is adjacent to the free surface. Thus, the velocity correction equation for u can be written as

$$u=u^*+h^*(B^u H_\xi'+C^u H_\eta'). \tag{35}$$

A similar equation can be written for v:

$$v=v^*+h^*(B^v H_\xi'+C^v H_\eta'). \tag{36}$$

Hence, the corrections to the contravariant velocity components U and V can be obtained by substituting equations (35) and (36) into equations (21) and (22), which yields

$$U = U^* + h^*(B^u y_\eta - B^v x_\eta) H'_\xi + h^*(C^u y_\eta - C^v x_\eta) H'_\eta \tag{37}$$

and

$$V = V^* + h^*(C^v x_\xi - C^u y_\xi) H'_\eta + h^*(B^v x_\xi - B^u y_\xi) H'_\xi. \tag{38}$$

The last terms in equations (37) and (38) may also be set to zero without affecting the converged solution, since H' is extremely small when the criterion of convergence is satisfied. The corrections for the contravariant velocity components can thus be rewritten as

$$U = U^* + BH'_\xi \tag{39}$$

and

$$V = V^* + CH'_\eta, \tag{40}$$

where

$$B = -\left(\frac{y_\eta^2}{A_p^u} + \frac{x_\eta^2}{A_p^v}\right)\frac{\rho g h^*}{J}\Delta\xi\,\Delta\eta \tag{41}$$

and

$$C = -\left(\frac{y_\xi^2}{A_p^u} + \frac{x_\xi^2}{A_p^v}\right)\frac{\rho g h^*}{J}\Delta\xi\,\Delta\eta. \tag{42}$$

Since the condition of continuity must also be satisfied for the overall water depth, the water depth correction equation is obtained by substituting equations (39) and (40) into the continuity equation (27). Its final form is given by

$$\sum_{l=1}^{l_{max}} (A_p^H)_l H'_p = \sum_{l=1}^{l_{max}} (A_N^H)_l H'_N + \sum_{l=1}^{l_{max}} (A_S^H)_l H'_S + \sum_{l=1}^{l_{max}} (A_E^H)_l H'_E + \sum_{l=1}^{l_{max}} (A_W^H)_l H'_W + \sum_{l=1}^{l_{max}} (M_H)_l, \tag{43}$$

where

$$A_E^H = (J\rho h B\,\Delta\eta)_E, \tag{44}$$

$$A_W^H = (J\rho h B\,\Delta\eta)_W, \tag{45}$$

$$A_N^H = (J\rho h C\,\Delta\xi)_N, \tag{46}$$

$$A_S^H = (J\rho h C\,\Delta\xi)_S, \tag{47}$$

$$A_P^H = A_E^H + A_W^H + A_N^H + A_S^H \tag{48}$$

and

$$M_H = (J\rho h U^*\Delta\eta)_w - (J\rho h U^*\Delta\eta)_e + (J\rho h V^*\Delta\xi)_s - (J\rho h V^*\Delta\xi)_n. \tag{49}$$

In equation (49), M_H is the local imbalance of mass resulting from the incorrect velocity field. When the value of M_H reaches zero, the water depth correcting procedure is completed. After correcting H', U' and V', one must recalculate the vertical velocity w at the interfaces according to the continuity equation (26).

Since the non-staggered grid system is used in the model, the 2-Δ second-order difference scheme does not sense the pressure oscillation at the 1-Δ grids.[22] The remedy is to relocate the

contravariant velocities at the grid surface, which are related to the local convective terms. From equations (21), (28) and (29) the contravariant velocities U at points P, E and at the control surface 'e' can be written as

$$U_P = D_P + (BH_\xi)_P, \tag{50}$$

$$U_E = D_E + (BH_\xi)_E \tag{51}$$

and

$$U_E = D_E + (BH_\xi)_E, \tag{52}$$

where

$$D = \frac{y_\eta}{JA_P^u}\left(\sum_{n=E,W,N,S} A_n^u u_n + S^u\right) + \frac{X_\eta}{JA_P^v}\left(\sum_{n=E,W,N,S} A_n^v v_n + S^v\right) + \frac{h}{J}(C^u y_\eta + C^v x_\eta) H_\eta. \tag{53}$$

At the east control surface of each layer, the velocity U_e may also be obtained by linear interpolation of U_P and U_E. Its approximate form is given by U_e as

$$\tilde{U}_e = \tilde{D}_e + \tilde{B}_e(\tilde{H}_\xi)_e. \tag{54}$$

Substituting this equation into equation (52) yields

$$U_e = \tilde{U}_e + \tilde{B}_e[(H_\xi)_e - (\tilde{H}_\xi)_e], \tag{55}$$

where

$$(H_\xi)_e = \frac{H_E - H_P}{\Delta\xi}. \tag{56}$$

For the estimated field, equation (55) is expressed as

$$U_e^* = \tilde{U}_e^* + \tilde{B}_e[(\tilde{H}_\xi^*)_e - (\tilde{H}_\xi^*)_e]. \tag{57}$$

By this modification to the contravariant velocities in the source term of the water depth correction equation, the oscillations in the pressure field were found to be successfully suppressed.

Based on the derived algebraic equations, a solution procedure similar to the usual SIMPLE approach is used to obtain convergent solutions. The convergent criteria is set at 1×10^{-4} for the non-dimensional overall residual.

4. MODEL VALIDATION

Three test cases were used to validate the numerical model: (1) flow in a 180° channel bend, (2) flow near a groin and (3) flow in a straight open channel with the emphasis on computing the distribution of the energy dissipation rate to check the ability of turbulence modelling. These three cases are discussed in the following sections.

Case 1: steady flow in a 180° channel bend

In 1977, De Vriend[24] performed experiments at the Laboratory of Fluid Mechanics (LFM) in the Department of Civil Engineering, Delft University of Technology in Holland. The experimental channel was a 180° bend with a centreline radius of 4·25 m. The inlet and outlet of the bend were connected to straight reaches of 6 m long, and the channel width B was 1·7 m. The channel boundaries were smooth and a Chezy's coefficient C of 57 $m^{1/2}/s$ was reported.

One of the LFM's experiments, having a discharge of 0·19 m^3/s, with a depth of 0·18 m maintained by a weir at the downstream end of the flume, was simulated using the present model. The computations were performed with a six-multilayered (6 ML) model and a depth-averaged (DAV) k ε model, both with the 80×40 automatically generated mesh system shown in Figure 3. Comparisons of the water surface elevations between the numerical predictions and LFM's experimental data are presented in Figure 4. The longitudinal distance from the inlet is normalized by the length at centre of the bend and shown as S in the figure. The deviation of water surface from that at the downstream end of the bend is normalized by the total depth at the channel outlet and denoted by $\bar{H}$. The water deviations obtained from the LFM's experiments are indicated by the symbols +, ○ and □, which represent the values at the centre, at $B/10$ from the outer bank, and $B/10$ from the inner bank, respectively. The averaged water surface deviation $\bar{H}_{av}$ for the whole channel bend is 0·05.

In Figure 4(a), the $\bar{H}$ values within the bend predicted by the depth-averaged k–ε model do not agree with the experiments. At the centre and B/10 from the inner bank, the water surfaces are underestimated in the regions of S between 0·3 and 0·7. The largest and root mean square deviations between the measured and simulated values are 63·1 and 25·0% of $\bar{H}$, respectively. Attempts had been made to improve the DAV model by replacing the power-law scheme with the Quick scheme[25] and by adding a local equilibrium modified term[8] to the turbulence energy dissipation equation. The modifications did not significantly improve the results. The multi-layered model calculation shown in Figure 4(b), which takes the effect of the secondary flow motion into account, shows the improvements in the prediction of $\bar{H}$. The largest and root mean square deviations between the measured and simulated $\bar{H}$ values have reduced to 37·3 and 18·4% of $\bar{H}$, respectively. The cross-sectional water surface elevation crossing and recrossing the centreline along the channel bend is observed in the regions of $0{\cdot}75 \leq S \leq 0{\cdot}85$. The prediction of the depth-averaged model does not show this particular phenomena. It indicates that the first type secondary flow around the bend is important and should be considered. The present 6ML model is just enough to sense this 3D effect. Further inspections on the water surface have observed no oscillation and indicate that the water depth correction method can be used in the depth-averaged and the multi-layered turbulent flow models.

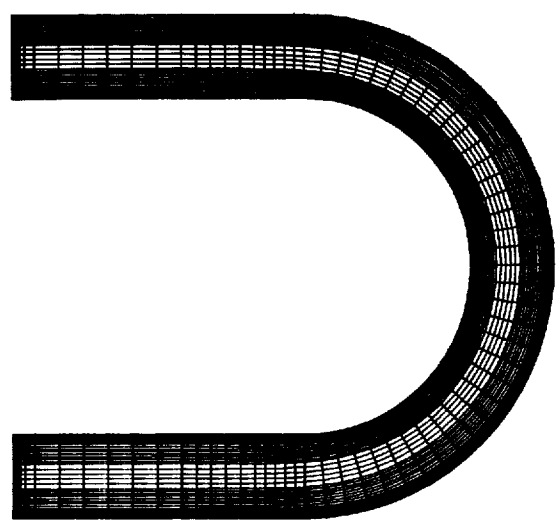

Figure 3. Computational mesh (80×40) for 180 channel bend

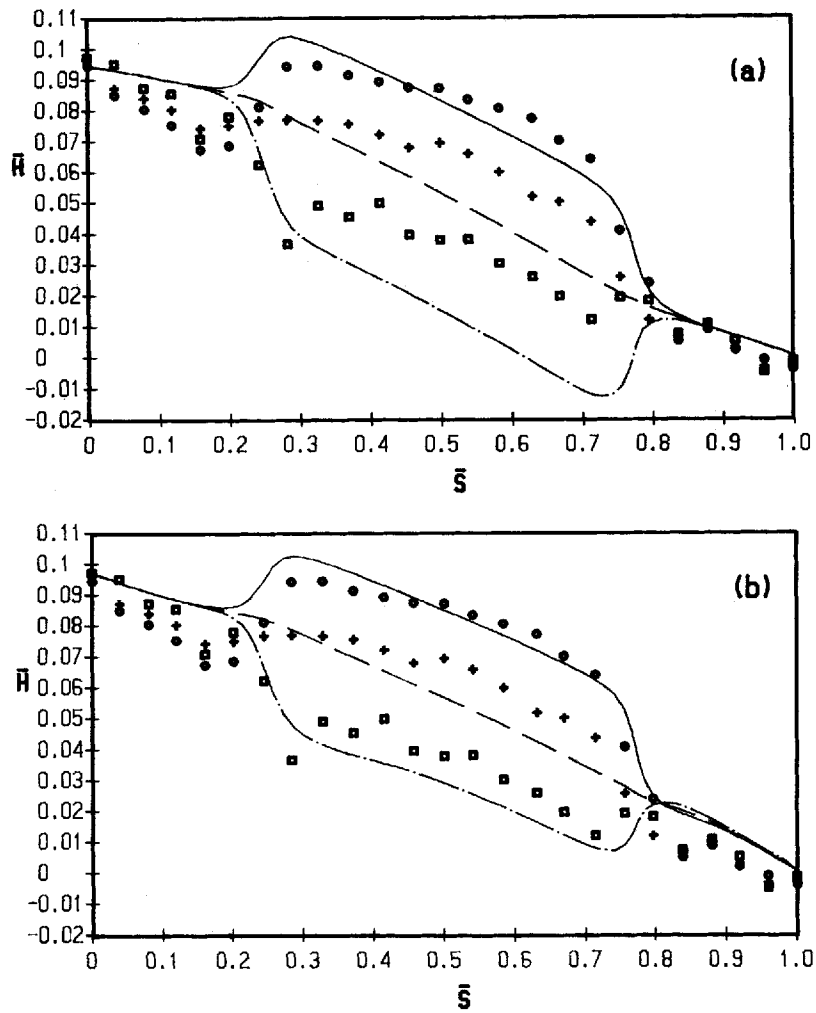

Figure 4. Computed and observed[24] water surface elevations along channel bend: (a) DAV (b) 6ML. —— O−B/10; – – centre; — · — I+B/10

Case 2: steady flow near a groin in a straight open channel

Rajaratnam and Nwachukwu,[26] R&N conducted a series of experiments on turbulent flows near a groin in a straight rectangular channel. The channel was 37 m long, 0·915 m wide and 0·76 m deep, with smooth boundary. The groin was located in the downstream half of the channel, and the water depth was kept constant with a weir at the downstream end of the channel.

Computations were made for two tests, A1 and A2. The discharges for the two tests were 0·0432 and 0·0449 m^3/s, with depths at the downstream end of 0.189 and 0·223 m, respectively. The length of the groin for both cases was 0·152 m. A 80×40 grid system shown in Figure 5 was used for the computations. The computed non-dimensional depth-averaged velocity and bottom shear stress distributions are shown from Figures 6–8. In the figures, the non-dimensional velocities are given as U/U_0, where U_0 is the cross-sectional depth-averaged longitudinal velocity at the

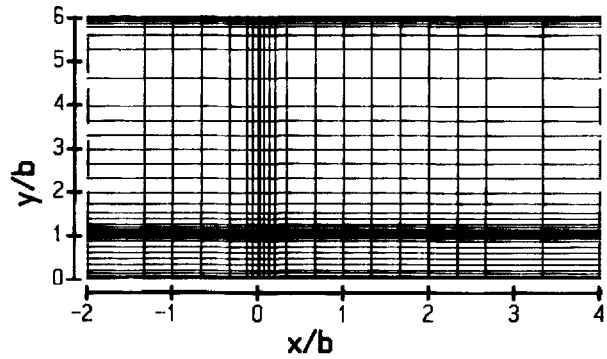

Figure 5. Computational mesh (80 × 40) for channel with groin located at $x/b=0$

downstream end, x is the distance along the channel with the origin at the groin, y is the perpendicular distance from the bank and b is the length of the groin.

For comparing, the data reported by Tingsanchali and Maheswaran[9] (T&M) for the experiments A2 of R&N are indicated by the symbol ○. The calculated results of T&M, using a staggered depth-averaged model with corrections for the calculations, are also plotted. The corrections of T&M included: (i) a corner correction at the tip of the groin, (ii) the correction for the streamline curvature, LPS and (iii) the friction coefficient correction for the 3D effect. Symbol S2 represents the predictions of T&M by using the corner and LPS corrections, and symbol S3 represents the results of T&M with all the three corrections. The present DAV and 6ML model calculations use the standard k–ε model without any correction.

The results of the 6ML and DAV models shown in Figure 6 indicate that they agree well with the A2 experiment at the section upstream of the groin, ($x \leq b \leq 0$), and are better than the predictions of T&M (S3) at the near-wall region. Just behind the groin, the flow is redeveloping, and all the calculations deviate from the A2 results. The 6ML and DAV models tend to underestimate, while T&M (S3) overpredict the near-wall reverse velocities. The largest error occurs at $0{\cdot}5 \leq y/b \leq 1{\cdot}0$. Data of R&N show that the largest reverse velocities occur at y/b around 0·5 at sections $x/b=2$, 4 and 8, but both T&M and the 6ML models predict a maximum reverse velocity very close to the wall.

The 3D structure of the flow near the groin can be seen from the velocity vectors at the bottom, second and fifth layers plotted in Figure 7(a)–(c). The plot for the bottom layer shows a region of strong reverse flow in front of the groin, *I*, which becomes weaker at the fifth layer. Depth-averaged vectors shown in Figure 7(d) also has a small recirculation region *I*, and the recirculation zone, *II*, is smaller than that of the bottom layer.

The bottom shear stress (τ_b) distribution for experiment A1, with three groups of computed results, are compared in Figure 8. The bottom stress shear stress τ_{bo} is measured at 0·92 m upstream of the groin on the centreline of the channel. In the region upstream of the groin ($x/b<0$, $y/b>1$) where the 3D effect was not significant, the three computed results agree quite well the data of experiment A1. At the tip of the groin ($x/b=0$ and $y/b=1{\cdot}0$) the prediction of S3 is the best. In the region of y/b between 1·5 and 4·0 downstream of the groin, the 6ML model shows better predictions than S2 or S3 of T&M.

According to the wall shear stress distribution, the reattachment length is also estimated. The predicted values for the 6ML and DAV are 11·5b and 8·0b, which are 8 and 36% less than the measurement of R&N, 12·5b. Since the 6ML model has taken the 3D effects into account for

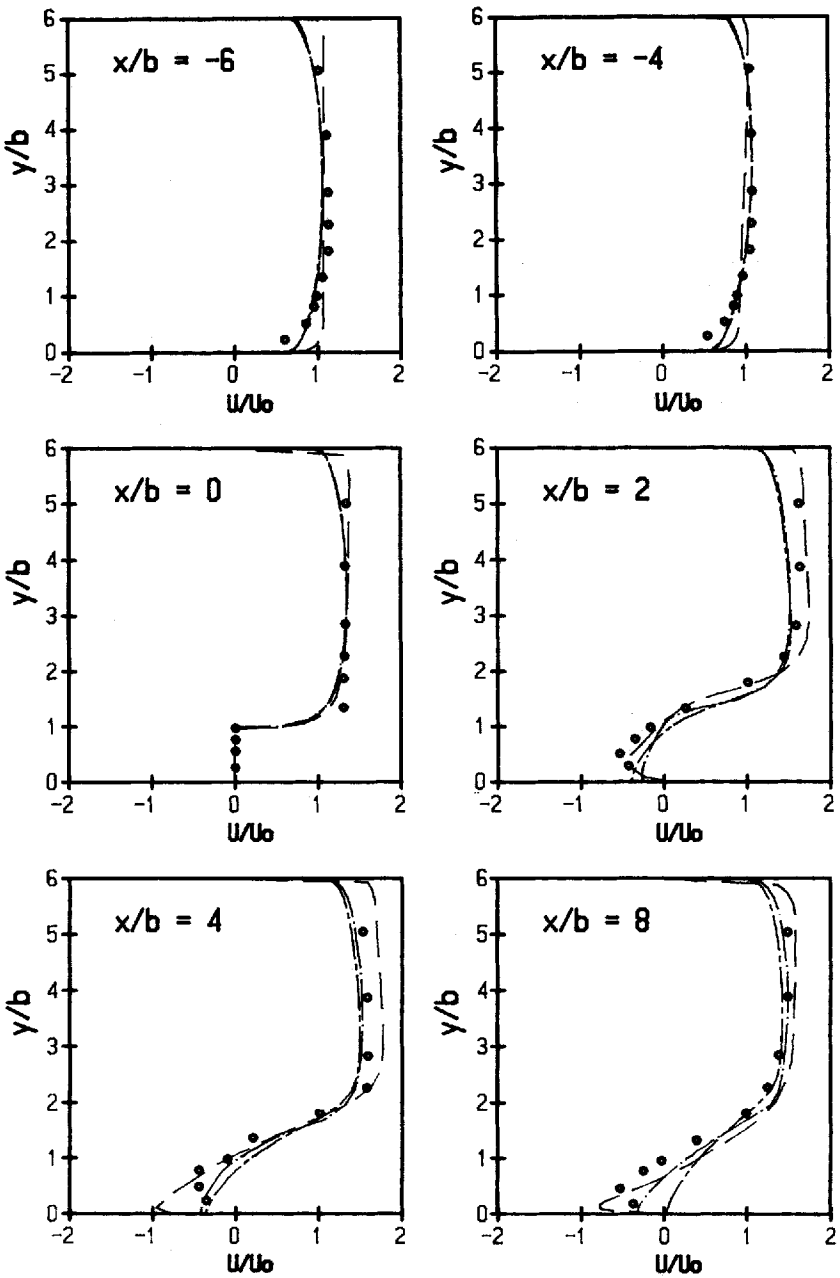

Figure 6. Lateral velocity profiles in open channel (groin located at $x/b = 0$); ◦ experiments;[25] — · — 6ML; — - — DAV; – – S3, T&M[9]

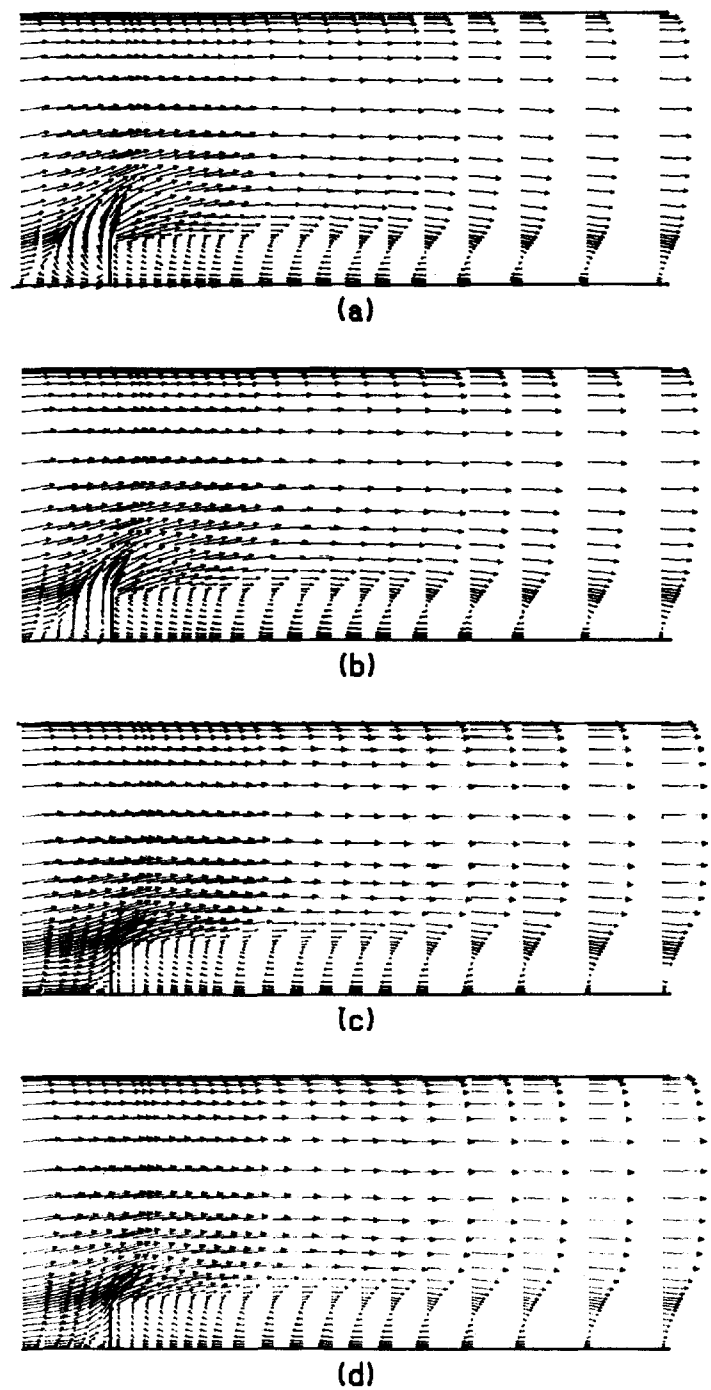

Figure 7. Computed lateral velocity fields using the 6ML model: (a) first layer; (b) second layer; (c) fifth layer; (d) depth-averaged flow pattern

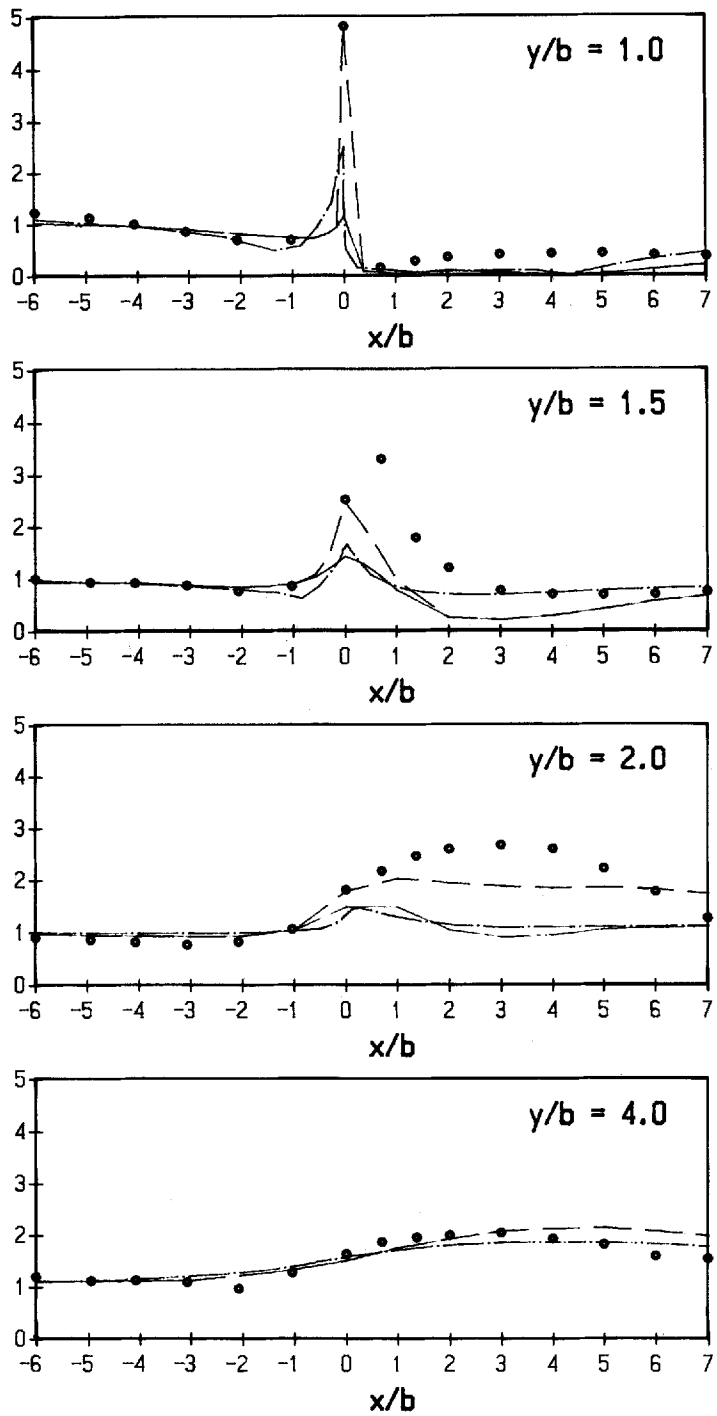

Figure 8. Bed shear stress distributions along channel (groin located at $x/b=0$); ◦ experiments[25] — · — 6ML; —— S2, T&M[9]; – – S3, T&M[9]

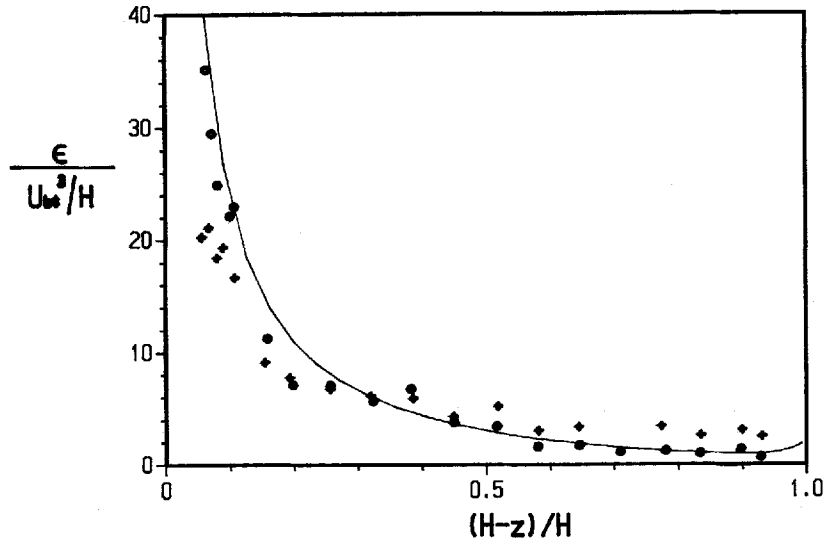

Figure 9. Vertical distribution of energy dissipation rate in open channel: —— present calculation; data of Nakagawa *et al.*[27] ◦ Kolmogoroff approach; + isotropy approach

the velocity redevelopment and shear stress computation. Thus, it yields, without any correction, the results as good as those predictions of the DAV models with empirical corrections.

Case 3: turbulent energy dissipation rate in a straight channel

Using the experimental data reported by Nakagawa *et al.*[27] for turbulent flow in a smooth straight open channel, the turbulence quantities were calculated using the present multilayer model. Since turbulent energy dissipation rate is an important parameter in the dynamics of turbulent flow and is a good check for the present model. The calculated energy dissipation rates are normalized and shown as a solid line in Figure 9. The data deduced from the Kolmogroff and isotropic approaches reported by Nakagawa *et al.* are also plotted for comparison. In general, the calculated results are in good agreement with the data of using the Kolmogroff approach. An increasing in ε near the free surface is also observed. Similar result had been reported by Baumart and Radach.[28]

5. DISCUSSIONS

Comparisons with experimental and other model results indicate that the present multilayer model is capable of simulating turbulent flow, both the mean flow and the turbulent quantities in an open channel. The use of a general co-ordinate and non-staggered grid system increases the ability of the present model in computing complex 3D flows. Also, the structure of the model is similar to that of a depth-averaged model, which means that a nested model can be easily constructed; to couple a 2D flow problem with local 3D refinement,[4] for example.

Although the present multilayer model has significantly improved the prediction of the recirculation region, it still underestimates the reattachment length. Whether this underestimation is the result of using the standard k–ε turbulence model, as noted by the ASCE Task Committee,[2] should be further tested. On the ther hand, the experimental data available for

turbulent open-channel flow validation, particularly the turbulent quantities near the solid boundary and free surface, are still lacking. It is thus needed to conduct more detailed measurements of the turbulent quantities using Laser Doppler Anemometer (LDA) so the turbulence model with free-surface effect can be further refined.

6. CONCLUSIONS

A multilayer model has been developed to simulate turbulent flow in an open channel with arbitrary boundary shapes. The grid pattern is non-staggered and is imposed on a general curvilinear co-ordinate system.

Comparisons of the calculated results with experimental data in a straight channel show that the present multilayer formulation with the standard layer averaged k–ε model sufficiently yields the good predictions both of the mean flow and turbulent quantities. The water depth correction scheme can be used to obtain the free-surface elevation, avoiding the rigid-lid assumptions, and eliminating the oscillation of the calculations due to the non-staggered grid arrangement. For strong recirculating flow, the multilayer model is shown to have improved the predictions significantly but still has its limitations. To improve the performance of the present model, the refinements of the turbulence model and the collection of more open-channel flow data for validation of the model are both required.

APPENDIX: NOTATIONS:

A_E, A_N, A_W, A_S	coefficients in finite difference equations
B^u, B^v, C^u, C^v	coefficients for velocity correction
B	width of flume
b	length of groin
$C_\mu, C_1, C_2,$ $\sigma_k, \sigma_\varepsilon$	coefficients for turbulence model
C_f	friction coefficient
G	production of turbulent kinetic energy
g	gravitational acceleration
g^{ij}	metric tensor
H	overall water depth
$\bar{H}$	non-dimensional water surface deviation
h_l	water depth at layer l
h'	correction for water depth
J	Jacobian
k	turbulent kinetic energy
l_{max}	top layer
R^ϕ	source term of ϕ, physical plane
S^ϕ	source term of ϕ, computational plane
U, V	contravariant velocity in computational plane
u, v, x, y	velocities in physical domain
w	vertical velocity at interface
U_{b^*}	friction velocity at channel bed
U_{b^*}	friction velocity at side walls
U/U_0	non-dimensional velocity
y_w	distance from the wall used by the wall function

z	elevation downward related to the free surface
ϕ	general variable
κ	von Karman constant
Γ	diffusion coefficients
ε	turbulent kinetic energy dissipation rate
ξ, η	general curvilinear co-ordinates
μ_e	effective viscosity
μ	molecular viscosity
μ_t	eddy viscosity
ρ	fluid density
τ_{bo}	overall bed shear stress
τ_b	bed shear stress
τ_w	wall shear stress
τ_{bx}	bed shear stress in x direction
τ_{by}	bed shear stress in y direction
τ_{xx}, τ_{xy}	turbulent shear stress

REFERENCES

1. W. Rodi, 'Turbulence model and their application in hydraulics', *Monograph*, IAHR, Delft, 1980.
2. ASCE Task Com., 'Turbulence modeling of surface water flow and transport, Part II', *J. Hydraul Eng. ASCE*, **114,** 992–1014 (1988).
3. H. B. Fischer (Ed.), 'Transport models for inland and coastal waters' in *Proc. Symp. on Predictive Ability*, Academic Press, New York, 1981.
4. J. C. J. Nihoul and B. M. Jamart (Ed.), *Three-dimensional Models of Marine and Estuarine Dynamics*, Elsevier, Amsterdam, 1987.
5. A. K. Rastogi and W. Rodi, 'Predictions of heat and mass transfer in open channels', *J. Hydraul. Div. ASCE*, **104,** 397–420 (1978).
6. R. J. Keller and W. Rodi, 'Prediction of flow characteristics in main channel/flood plain flows', *J. Hydraul. Res.*, **26,** 425–441 (1988).
7. J. J. McGuirk and W. Rodi, 'A depth-averaged mathematical model for the near field of side discharges into open-channel flow', *J. Fluid Mech.*, **86,** 761–781 (1978).
8. C. J. Lai, C. W. Yen and Y. J. Jan, 'A versatile turbulent flow numerical model for hydraulic engineering', *Proc. Internat. Conf. on Computer Applications in Water Resources*, Tamsui, Taiwan, Vol. 1, 1991, pp. 251–259.
9. T. Tingsanchali and S. Maheswaran, '2-D depth-averaged flow computation near groin', *J. Hydraul. Eng. ASCE*, **116,** 71–86 (1990).
10. G. Raithby, R. Elliott and B. Hutchinson, 'Prediction of three-dimensional thermal discharge flows', *J. Hydraul. Eng. ASCE*, **114,** 720–737 (1988).
11. B. E. Launder, C. H. Priddin and B. I. Sharma, 'The calculation of turbulent boundary layers on spinning and curved surface', *J. Fluid Eng. Trans. ASME, Series D*, **99,** 231–239 (1977).
12. M. A. Leschziner and W. Rodi, 'Calculation of annular and twin parallel jets using various discretization schemes and turbulence-model variations', *J. Fluid Eng. Trans. ASME, Series D*, **103,** 352–360 (1981).
13. J. P. Johnston, 'On the three-dimensional turbulent boundary layer generated by secondary flow', *J. Basic Eng. Trans. ASME, Series D*, **82,** 233–248 (1960).
14. A. O. Demure and W. Rodi, 'Side discharges into open channels: mathematical model', *J. Hydraul. Div. ASCE*, **108,** 1707–1722 (1982).
15. D. Naot, and W. Rodi, 'Calculation of secondary current in channel flow', *J. Hydraul. Div. ASCE*, **108,** 948–968 (1982).
16. H. C. Chen, V. C. Patel and S. Ju, 'Solutions of Reynolds-averaged Navier–Stokes equations for three-dimensional incompressible flows', *J. Comput. Phys.*, **88,** 305–336 (1990).
17. R. W. Lardner and H. M. Cekirge, 'A new algorithm for three-dimensional tidal and storm surge computations', *Appl. Math. Modelling*, **12,** 471–481 (1988).
18. Y. Shimizu, H. Yamaguchi and T. Itakura, 'Three-dimensional computation of flow and bed deformation', *J. Hydraul. Eng. ASCE*, **116,** 1090–1108 (1990).
19. A. M. Davis, 'On formulating a three-dimensional hydrodynamic sea model with an arbitrary variation of vertical eddy-viscosity', *Comput. methods appl. mech. eng.*, **22,** 187–211 (1980).
20. N. S. Heaps and J. Jones, 'Three dimensional model for tides and surges with vertical eddy viscosity prescribed in two layers, II', *Geophys. J. R. Astron. Soc.*, **24,** 303–320 (1981).

21. S. V. Patankar and D. B. Spalding, 'A calculation procedure for heat, mass and momentum transfer in three-dimensional parabolic flows', *Int. J. Heat Mass Transfer*, **15**, 1787–1806 (1972).
22. C. M. Rhie and W. L. Chow, 'Numerical study of the turbulent flow past an airfoil with trailing edge separation', *AIAA J.*, **21**, 1525–1532 (1983).
23. B. E. Launder and D. B. Spalding, 'The numerical calculation of turbulent flows', *Comput. methods appl. mech. eng.*, **3**, 269–289 (1974).
24. H. J. De Vriend, 'A mathematical model of steady flow in curved shallow channels', *J. Hydraul. Res.*, **15**, 37–53 (1977).
25. B. P. Leonard, 'A stable and accurate convective modelling procedure based on quadratic upstream interpolation', *Comput. methods appl. mech. eng.*, **19**, 59–98 (1979).
26. N. Rajaratnam and B. Nwachukwu, 'Flow near groin-like structures', *J. Hydraul. Div. ASCE*, **109**, 463–480 (1983).
27. H. Nakagawa, I. Nezu and H. Ueda, 'Turbulence of open channel flow over smooth and rough beds', *Proc. JSCE*, **241**, 155–168 (1975).
28. H. Baumert and G. Radach, 'Hysteresis of turbulent kinetic energy in non-rotational tidal flows: a model study', *J. Geophys. Res.*, **97**, 3669–3677 (1992).